Exp Fluids (2011) 50:547–559
DOI 10.1007/s00348-010-0898-9

RESEARCH ARTICLE

Shockwave–turbulent boundary layer interaction control using magnetically driven surface discharges

Chiranjeev S. Kalra · Sohail H. Zaidi · Richard B. Miles · Sergey O. Macheret

Received: 28 October 2009 / Revised: 19 April 2010 / Accepted: 15 May 2010 / Published online: 18 August 2010

Abstract This study demonstrates the potential for shockwave–turbulent boundary layer interaction control in air using low current DC constricted surface discharges forced by moderate strength magnetic fields. An analytical model describing the physics of magnetic field forced discharge interaction with boundary layer flow is developed and compared to experiments. Experiments are conducted in a Mach 2.6 indraft air tunnel with discharge currents up to 300 mA and magnetic field strengths up to 5 Tesla. Separation- and non-separation-inducing shocks are generated with diamond-shaped shockwave generators located on the wall opposite to the surface electrodes, and flow properties are measured with schlieren imaging, static wall pressure probes and acetone flow visualization. The effect of plasma control on boundary layer separation depends on the direction of the Lorentz force ($j \times B$). It is observed that by using a Lorentz force that pushes the discharge upstream, separation can be induced or further strengthened even with discharge currents as low as 30 mA in a 3-Tesla magnetic field. If shock-induced separation is present, it is observed that by using Lorentz force that pushes the discharge downstream, separation can be suppressed, but this required higher currents, greater than 80 mA. Acetone planar laser scattering is used to image the flow structure in the test section and the reduction in the size of recirculation bubble and its elimination are observed experimentally as a function of actuation current and magnetic field strength.

C. S. Kalra (✉) · S. H. Zaidi · R. B. Miles
Applied Physics Group, Mechanical and Aerospace Engineering Department, Princeton University, Princeton, NJ 08544, USA
e-mail: ckalra@princeton.edu

S. O. Macheret
Lockheed Martin Aeronautics Company, Skunk Works, Palmdale, CA 93599-0160, USA

1 Introduction

Shockwave–turbulent boundary layer interactions (STBLI) are unavoidable in most internal and external flows associated with supersonic flight vehicles (Lin 2002). Of particular importance is shock-induced boundary layer separation, which leads to a local pressure increase and boundary layer thickening. These effects can further reinforce each other, inducing a flow instability which may lead to engine unstart and engine stall (Dolling 2001). Separation can occur in front of compression corners in ducts and along duct walls near points of oblique shockwave reflection, both of which are characteristic of RAM and SCRAM jet inlets, isolators, and combustors. Effective control of boundary layer separation can lead to increased performance and higher efficiency (Lin 2002) as well as to safer operation. In the case of a weak shockwave interaction with the turbulent boundary layer, separation does not occur. However, as the shock strengthens a recirculation bubble forms, driven by the high pressure behind the shock and moving upstream along the wall in the subsonic portion of the flow. This bubble lifts the boundary layer in front of the shock and moves the shock intersection point upstream.

Figure 1, taken from Delery and Marvin (1986), shows this interaction for both the non-separated condition (a) and the separated condition (b). In both cases, the incoming oblique shock extends into the boundary layer with varying strength and inclination and ends at the sonic line, resulting in a pressure profile at the wall that is necessarily continuous. This results in a thickening of the subsonic part of the

boundary layer that extends upstream as well as downstream of the interaction point. In Fig. 1a, an incoming oblique shockwave (C1) in the core flow with Mach number (Mo) interacts with the turbulent boundary layer (δ), resulting in a thickening of the boundary layer and the production of compression waves (l1 and l3) that generate the reflected shock (C2). In Fig. 1b, the incident oblique shockwave (C1) is strong enough to cause recirculation and separation. The reflected shock is generated due to boundary layer thickening and starts well upstream of the point where C1 hits the boundary layer. This reflected shock interacts with the incident shockwave (C1) resulting in refracted shocks (C3) and (C4) and the production of a slip line. The recirculation zone produces a gradual pressure rise upstream of the shock impingement point and a *plateau* is observed in the wall static pressure profile between the initial pressure rise at the leading edge of the recirculation bubble and the final pressure rise downstream. In the case of separation, the boundary layer thickening is significantly greater than for a non-separated interaction. In an inlet or duct, this thickening of the boundary layer reduces the effective cross section and may choke the flow, leading to engine unstart. These shockwave–boundary layer interactions are independent of the flow geometry and the particular method of shock generation, thus they are termed *free interactions* by Chapman et al. (1958).

Boundary layer separation control can be achieved using many different approaches, all of which modify the flow near the surface. Passive methods for boundary layer control include vortex generators, surface cavities, riblets, and boundary layer venting methods. On the other hand, active boundary layer control methods consist mainly of energy addition to the flow in some form, such as periodic flow excitation by morphing surfaces, synthetic jets and plasma actuators. The most successful method of passive separation suppression is through the use of low profile vortex generators. McCormick et al. (1992) have proven that when these are placed upstream of the shock impingement point the extent of the separation region is significantly reduced. For active control of separating flows the use of synthetic jets, mainly in the form of plasma actuators, has generated significant interest (Kral 1999; Opaits et al. 2007; Jesse et al. 2009). The main advantages of active control using plasma actuators are that they do not add drag since they are flush mounted, they can only be operated when needed, and they can perform at optimized response frequencies.

Magnetohydrodynamic (MHD) methods of boundary layer control in high-speed flows are being actively studied by a number of groups (Gaitonde 2008; Nishihara et al. 2005; Lineberry et al. 2002; Fujino et al. 2004; Shang et al. 2005). When a magnetic field is imposed on a weakly ionized plasma created in the boundary layer, it affects both the plasma and the flow, through the $\bar{j} \times \bar{B}$ body force. The flow is also affected by the Joule heating produced by the plasma. The body force effects have been proposed for flow separation control (Lineberry et al. 2002) and experimentally shown to be capable of modifying turbulence (Munetake et al. 2005). Joule heating in the near-surface plasma was also shown to affect supersonic flows through gas displacement and viscous–inviscid interactions (Shang et al. 2005).

2 Plasma-boundary layer interaction: analytical model

In this section, the physics of constricted, moving non-equilibrium DC discharges between surface embedded electrodes is analyzed. In the experiments, a cold constricted plasma discharge is generated between two slightly diverging copper alloy electrodes embedded in the surface. The electrodes are oriented so that the discharge is formed across the flow and they diverge either in the downstream direction for separation suppression or in the upstream direction for separation enhancement. The discharge initiates at the point where the electrodes are closest and moves either downstream or upstream until it passes beyond the electrodes and extinguishes as a new discharge initiates at the closest point. The closest distance between the electrodes is 1.1 cm, and a constant current of between 35 and 300 mA is sustained in a current stabilized mode. The static pressure in test section is 30 Torr, and the free stream flow temperature is about 140 K. At a constant current of 35 mA, the voltage drop across the electrodes is between

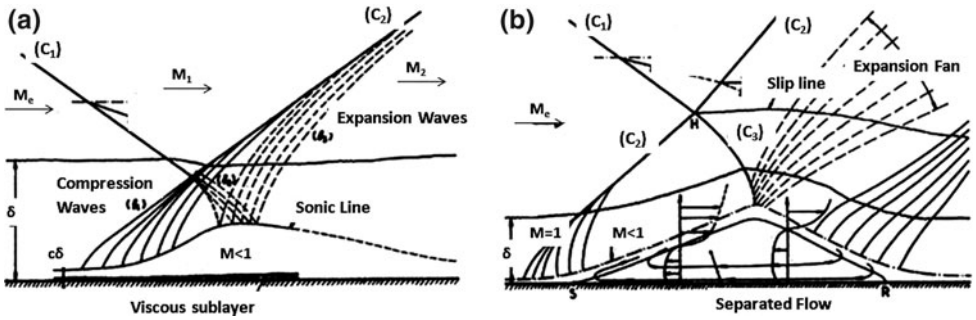

Fig. 1 Oblique shockwave reflection from turbulent boundary layer (Delery and Marvin 1986)

1.5 and 1.7 kV, depending on magnetic field strength. Since the cathode voltage drop can be as high as 300–400 V (Raizer 1997), the electric field normal to the electrodes in the positive plasma column is about 1.2 kV/cm. In experimental observations, in the presence of the magnetic field, the plasma column is canted at an angle of $\theta = 60$–$70°$ with respect to the streamwise direction. With a gas number density of $n = 1.05 \times 10^{18}$ cm^{-3} in the boundary layer, the ratio $[E/n]_{\text{eff}} \approx E\cos\theta/n \approx 1.1 \times 10^{-15}$ V cm^2 corresponds to an electron temperature $T_e = 2.3$–3 eV and to a condition where electron impact ionization is balanced by recombination and attachment losses of electrons (Raizer 1997). The electron–molecule and ion–molecule collision frequencies at the boundary layer density are estimated to be $\nu_{\text{en}} = 1.4 \times 10^{11}$ s^{-1}; $\nu_{\text{in}} = 1.15 \times 10^9$ s^{-1}. At a typical magnetic field strength of 2 Tesla, the electron and ion Hall parameters are $\Omega_e = \frac{eB}{m\nu_{\text{en}}} = 2.5$ and $\Omega_i = \frac{eB}{M'\nu_{\text{in}}} = 1.16 \times 10^{-2}$, where m is the mass of electron and M' is the ion–molecule reduced mass. The ion slip parameter is $\Omega_e\Omega_i = 2.9 \times 10^{-2}$. Further, the current density in the plasma column is approximately $j = 4.45 \times 10^4$ A/m^2, the electrical conductivity is $\sigma = j/(E \sin\theta) = 0.45$ mho/m, and from the expression (Raizer 1997), $\sigma = \frac{e^2 n_e}{m\nu_{\text{en}}}$, the electron number density can be estimated as $n_e \approx 2 \times 10^{12}$ cm^{-3}. The radius of the constricted plasma column can be estimated as $r \approx \sqrt{D_a\tau}$, where $D_a = \frac{eT_e}{M'\nu_{\text{in}}}$ is the ambipolar diffusion coefficient and τ is the electron lifetime. Under the conditions considered here, $\tau = (k_{\text{dr}} n_e)^{-1} \approx 2 \times 10^{-6}$ s, and $k_{\text{dr}} = 2.5 \times 10^{-8}$ cm^3/s is the dissociative recombination rate coefficient, giving the radius of plasma column as $r = 0.5$ mm, which agrees well with experimental observation.

2.1 Plasma column velocity

The physics of plasma column motion in transverse electric and magnetic fields can be described as follows: Electrons and ions drifting along the plasma column in the applied external electric field experience Lorentz forces normal to their drift velocities and to the magnetic field. Since the electron drift velocity greatly exceeds the ion drift velocity, the electrons begin to pull away from the ions in the direction of the Lorentz force. This quickly establishes polarization of the plasma column and the polarization electric field 'glues' electrons and ions together, so that they move as a whole. Both electrons and ions experience the friction force against the neutral gas, proportional to the difference of the plasma velocity $\vec{u_p}$ and the gas velocity $\vec{u}$. Considering the force balance for electrons in the reference frame moving at the plasma velocity, $\vec{u_p}$, greater than the gas velocity $\vec{u}$, Fig. 2 illustrates the forces on an electron moving with drift velocity $\vec{V_e}$: the Lorentz force $\vec{F_B} = -e\vec{V_e} \times \vec{B}$, the force due to the external field

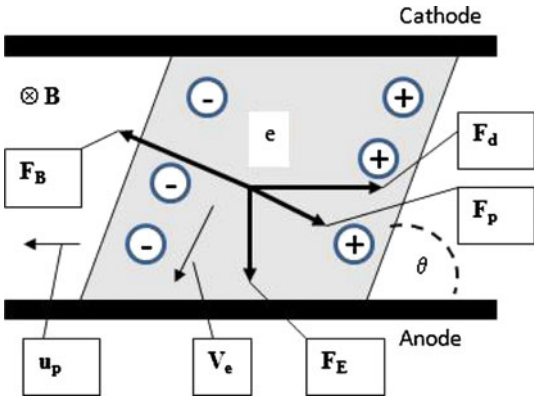

Fig. 2 Force balance for the electrons in the reference frame moving at plasma velocity $\vec{u_p}$, greater than the gas velocity $\vec{u}$

$\vec{F_E} = -e(\vec{E} + \vec{u_p} \times \vec{B})$, the force due to polarization electric field $\vec{F_p} = -e\vec{E_p}$, where $\vec{E_p}$ is the polarization electric field, and the drag force $\vec{F_D} = -mv_{en}(\vec{u_p} - \vec{u})$. Note that the conventional drag force does act against the drift velocity $\vec{V_e}$, but is not shown in figure.

The force balance for the electrons in the direction perpendicular to the plasma column is:

$$V_e B + (E - u_p B)\cos\theta = E_p + \frac{mv_{en}}{e}(u_p - u)\sin\theta \tag{1}$$

and the electron drift velocity along the plasma column is

$$V_e = \frac{e}{mv_{en}}(E - u_p B)\sin\theta + (u_p - u)\cos\theta \tag{2}$$

Similarly for ions, the force balance equation is given as

$$V_i B + E_p = (E - u_p B)\cos\theta + \frac{M'v_{in}}{e}(u_p - u)\sin\theta \tag{3}$$

with the ion drift velocity

$$V_i = \frac{e}{M'v_{in}}(E - u_p B)\sin\theta + (u_p - u)\cos\theta \tag{4}$$

From the force balance Eqs. 1–4 and the definitions of the electron and ion Hall parameters, the polarization field and plasma velocities can be calculated as follows:

$$\begin{aligned} E_p =& (\Omega_e \sin\theta + \cos\theta)\frac{(E - uB)\left(1 + 2\frac{\Omega_e\Omega_i}{\Omega_e+\Omega_i}\cot\theta\right)}{1 + \Omega_e\Omega_i + 2\frac{\Omega_e\Omega_i}{\Omega_e+\Omega_i}\cot\theta} \\ &- (\sin\theta + \Omega_e\cos\theta)\frac{\Omega_i(E - uB)}{1 + \Omega_e\Omega_i + 2\frac{\Omega_e\Omega_i}{\Omega_e+\Omega_i}\cot\theta} \end{aligned} \tag{5}$$

The plasma velocity is given as:

$$u_p = \frac{\Omega_e\Omega_i\frac{E}{B} + u\left(1 + 2\frac{\Omega_e\Omega_i}{\Omega_e+\Omega_i}\cot\theta\right)}{1 + \Omega_e\Omega_i + 2\frac{\Omega_e\Omega_i}{\Omega_e+\Omega_i}\cot\theta} \tag{6}$$

For typical conditions of interest, the following inequalities are satisfied: $\Omega_e \geq 1 \gg \Omega_i$; $\cot\theta \leq 1; \Omega_e\Omega_i \ll$

1; $E \gg uB$. Then, the relations for polarization field and plasma column velocity can be simplified as

$$E_p \approx \Omega_e E \sin\theta \tag{7}$$

$$u_p \approx \frac{\frac{E}{B}\Omega_e\Omega_i + u}{1 + \Omega_e\Omega_i} \approx \frac{E}{B}\Omega_e\Omega_i + u \tag{8}$$

Note that the plasma column velocity above does not depend explicitly on the canting angle θ. The ratio E/B in the plasma velocity relation above is the well known velocity of particle drift in crossed electric and magnetic fields in the absence of collisions, and the effect of collisions is represented by the ion slip parameter $\Omega_e\Omega_i$. In very strong magnetic fields and/or at very low gas densities, when $\Omega_e\Omega_i \gg 1$, the plasma column would move, according to relation above, at velocities approaching E/B. Under more practical and typical conditions, when $\Omega_e\Omega_i \ll 1$, the plasma column velocity with respect to the gas is reduced by collisions, down to the value of approximately $\frac{E}{B}\Omega_e\Omega_i$.

Using this equation, the plasma velocity is computed for the experimental parameters discussed in the last section as a function of magnetic fields up to 4 Tesla and compared with velocity measurements done in the Mach 2.8 wind tunnel experiments using a high-speed camera. Figure 3 shows the plot of this data, and there is good agreement between analytical estimations and observed values of plasma column velocity. When the magnetic field is strong enough and its polarity is reversed, the plasma column can be driven upstream, against the flow. The plasma velocity in this case can be calculated in a manner similar to Eq. 8:

$$u_{p,\text{upstream}} \approx \frac{\frac{E}{B}\Omega_e\Omega_i - u}{1 + \Omega_e\Omega_i} \approx \frac{E}{B}\Omega_e\Omega_i - u \tag{9}$$

In particular, at a certain value of magnetic field $B = B_o$, the plasma column will stop moving: the Lorentz force will be balanced by the drag created by the moving gas. From the equation above, the critical value of B_o can be estimated as $B_o = 0.34$ Tesla at 35 mA current, which, given the uncertainties of both theoretical estimates and experiments, is in fair agreement with the value $B_o = 0.23$ Tesla observed in experiments.

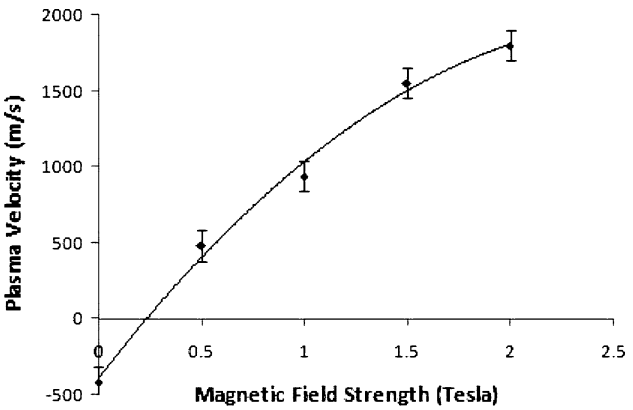

Fig. 3 Upstream plasma column velocity as a function of the magnetic field in experiments compared with analytical model results

2.2 Momentum and heat transfer to neutral gas flow

The moving plasma column acts as a porous piston while moving faster than the surrounding gas, and accelerates gas molecules that experience collisions with the charged particles. Although the molecule–electron collision frequency is two orders of magnitude greater than the molecule–ion collision frequency, the momentum carried by an ion moving at the velocity u_p exceeds the momentum carried by electrons moving at the same velocity by more than 4 orders of magnitude due to the high electron to ion mass ratio. Therefore, momentum transfer to the neutral gas molecules is primarily due to ion–molecule collisions. Since at thermal energies the ion–molecule collision cross section is approximately $\sigma_{in} \approx 1.5 \times 10^{-14}$ cm^2 (Raizer 1997), and the ion number density is about $n_i \approx 2 \times 10^{12}$ cm^{-3}, the mean free path of the molecule with respect to ions is about 32 cm, which is much longer than the 1mm thickness of plasma column. Therefore, only a small fraction of molecules experience collisions with ions during a single sweep of the plasma, which justifies the porous piston analogy.

The drag force on a molecule inside the plasma column is given as

$$f = k_{in} n_i M'(u_p - u) \tag{10}$$

where $k - in \approx 1.1 \times 10^{-9}$ cm^3/s is the ion–molecule momentum transfer rate constant (Raizer 1997). Since the residence time of a molecule inside the plasma column is approximately $\Delta t \approx h/(u_p - u)$, where h is the thickness of the plasma column, and the molecular mass M is approximately twice the ion–molecule reduced mass M', the gas velocity increment in a single sweep of the plasma is

$$\triangle V_1 = 0.5 k_{in} n_i h \tag{11}$$

The single-sweep velocity increment using this approximation is $\Delta V_1 \approx 1$ m/s. However, as the gas element in the boundary layer slowly moves along the wall, it experiences many "hits" by the consecutive rapidly moving plasma columns. The number of these hits is approximately equal to the ratio of plasma column velocity and the average gas velocity. Denoting the initial gas velocity as V_o and the final gas velocity after plasma interaction as V, we obtain

$$V - V_o = \frac{u_p}{0.5(V + V_o)} \triangle V_1 \tag{12}$$

From Eqs. 12, taking into account 8 and 11, the net velocity increment is

$$V^2 - V_o{}^2 = 2u_p \triangle V_1 = \frac{\frac{E}{B}\Omega_e\Omega_i + u}{1 + \Omega_e\Omega_i} k_{in} n_i h \tag{13}$$

with $u \approx (V + V_o)/2$.

In addition to the mechanical work done by magnetically driven plasma column on the gas, joule heat is created by the current and dissipated into the neutral gas flow. The joule dissipation rate per unit volume can be given as

$$P_j = j^2/\sigma \tag{14}$$

The mechanical force acting per unit volume can be estimated as

$$P = jB \sin\theta(u_p - u) \tag{15}$$

Taking into account Eqs. 13–15, the ratio is $P/P_j = \Omega_e\Omega_i$. The ratio thus only depends on gas density and magnetic field strength, and, under typical experimental conditions, at $B = 2$ Tesla, $\Omega_e\Omega_i = 2.9 \times 10^{-2}$, less than 3 percent of the total energy goes into useful mechanical work (gas acceleration). However, it is important to note that not the entire joule dissipation rate goes into gas heating. At $(E/N)_{\text{eff}} = E\cos\theta/n \approx 1.1 \times 10^{-15}$ V cm^2, only a small fraction of P_j at about $\chi = 5$–$10\,\%$ appears as heat (Raizer 1997). Most of the discharge power at these values of $(E/n)_{\text{eff}}$ goes into vibrational excitation of nitrogen and excitation of electronic states of nitrogen (primarily $N_2(A^3\Sigma)$) and oxygen. Vibrational relaxation of nitrogen in a cold low-density plasma is primarily due to collisions with oxygen atoms, and the estimated relaxation time for the experimental conditions here is not shorter than 10 ms. Quenching of $N_2(A^3\Sigma)$ in collisions with oxygen molecules is fast, but most of the energy released in this process goes into oxygen dissociation, so that the actual heat release is limited by the recombination of oxygen and formation of ozone. The estimated characteristic time of this process again exceeds 10 ms. Therefore, most of the dissipated energy of the discharge is channeled into excited states whose energy is released well downstream of the interaction region.

Expressing mechanical work through the increment of kinetic energy of the flow with Eq. 13 and using Eqs. 14 and 15, together with the heating fraction χ, we obtain the gas temperature increment due to the interaction with the moving plasma column:

$$\triangle T = \frac{(V^2 - V_o{}^2)\chi}{2c_p\Omega_e\Omega_i} = \frac{u_p \triangle V_1 \chi}{c_p\Omega_e\Omega_i} \tag{16}$$

where $c_p = 1{,}000$ J/(Kg K) is the specific heat of air. For experimental conditions at $B = 2$ Tesla, the temperature increment given by Eq. 16 is very small, $\Delta T = 3.4$–6.8 K. At higher magnetic field strength and higher current, in the range of $B = 3$ Tesla, $I = 210$ mA, corresponding to an ion density of 1.1×10^{13} cm^{-3} and the temperature increment would increase to $\Delta T = 13.4$–26.8 K. Therefore, volumetric joule heating is not expected to affect significantly the boundary layer accelerating action of the magnetically driven plasma column. A more substantial heating of the boundary layer may be due to the heat transfer from the exposed surface imbedded electrodes and active cooling might be required to minimize that effect.

3 Experimental setup

A schematic of the experimental setup employed in this study is shown in detail in Fig. 4. The experimental setup

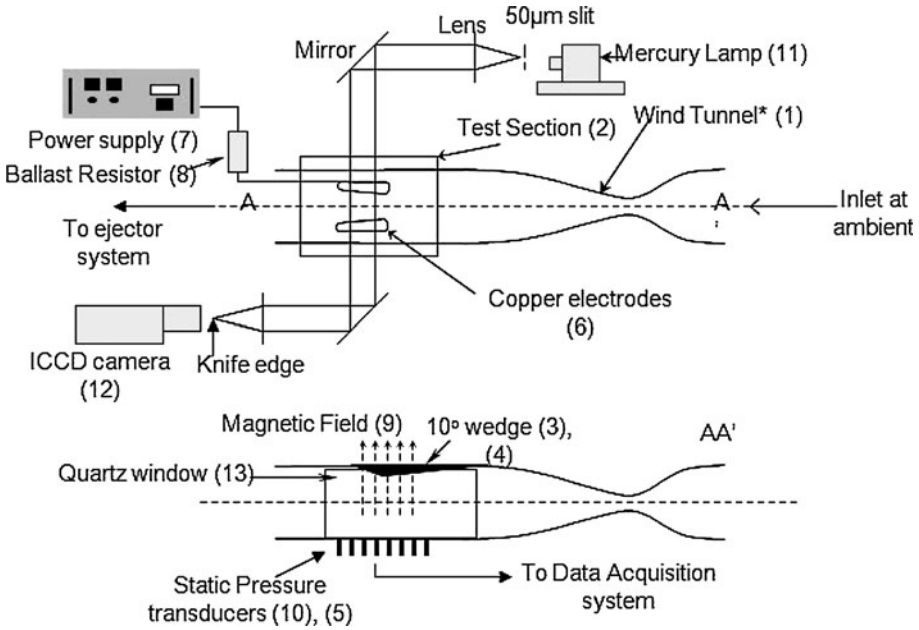

Fig. 4 Schematic of the experimental setup for the study of shockwave–boundary layer interaction and its control

consisted of a supersonic wind tunnel (1) with a constant cross-section test area. The wind tunnel used in this study was made of Lexan, with a rectangular test section (2) with a cross section of 1.25 × 2.0 inches. The tunnel operated as an in-draft facility with the flow driven by an external ejector system. The static pressure in the test section of the wind tunnel was measured to be 28 Torr. This gave a core flow operating Mach number of 2.8, corresponding to a free stream velocity of 660 m/s and temperature of about 140 K. The Reynolds number of the free stream flow inside the test section is estimated to be 7.0×10^5 and $Re_\theta \sim 10^4$, allowing for the assumption of fully developed turbulent boundary layer flow. A quartz window with dimensions 1.25 × 3.0 inches was mounted on the wall opposite to the electrodes for clear optical access to the test section for high-speed imaging of the plasma. Additionally, two quartz windows (13) of the same dimensions were mounted for Schlieren imaging of shockwave structure and of the interaction zone with turbulent boundary layer. The copper alloy electrodes (6) for generating the surface plasma were embedded in the wind tunnel surface and oriented in the streamwise direction in the test section. The shortest distance between the electrodes was 11 mm, diverging to 14 mm at a divergence angle along the streamlines of about 10 degrees. Static pressure ports (10) were placed at the surface at small distances intervals along the centerline. Honeywell microstructure pressure sensors (5) with an accuracy listed as 0.5 percent of measured value and a response time of less than 20 μs were employed for the measurement of the static pressure profile along the wall. A DC power supply (7) with a maximum voltage of 20 kV and 1,000 mA maximum current rating from Universal Voltronics was used to power the plasma. A ballast resistor (8) of 200 kOhm was used for currents lower than 35 mA, and above 70 mA, a 50 kOhm ballast was used.

In a typical experiment, a DC high voltage which was above the breakdown voltage at the shortest distance was applied to the electrodes. This caused a breakdown in the gap and the current increased rapidly to a few milliamperes (20–300 mA), and a plasma column formed across the electrodes. This plasma column was dragged downstream due to viscous forces of the flow in the boundary layer even in the absence of magnetic field. As the plasma column traveled along the electrodes, the voltage across the arc increased, resulting in higher power consumption. At the end of the electrodes, the plasma column was stretched and blown downstream. After a certain critical plasma column length, the voltage exceeded the breakdown voltage at the narrowest point, and another breakdown was initiated. The process naturally repeated at a frequency ranging from 10–100 kHz depending on current and magnetic field strength. The whole setup is placed in a magnetic field (9) which is perpendicular to surface such that, depending on the direction of magnetic field, B, and current, J, the plasma column generated between the electrodes experienced a force in either the upstream or the downstream direction. The magnet was an Oxford Instruments superconducting magnet with Helmholtz coils, capable of generating magnetic fields up to 7 Tesla.

A standard mercury lamp (11) illuminated the flow for Schlieren and shadow-graph imaging. A Princeton Instruments PI-MAX Intensified CCD camera (12) was used to capture an image of the plasma column as it passed either downstream or upstream. This camera was equipped with a 512 × 512 CCD array and the exposure time could be varied from the nanosecond range to the hundreds of milliseconds. It was triggered externally by a Stanford Research Systems digital timing box. A Princeton Scientific Instruments fast framing camera was also used to image the plasma column between the electrodes. This camera is capable of MHz rate operation and provides twenty eight sequential frames, capturing the movement of an individual plasma column streamer under various magnetic field strengths.

3.1 Experimental configurations

The different experimental configurations used in the study are shown in Fig. 5. In case 1 the electrodes are slightly diverging in the upstream direction, and the magnetic field forces the plasma column upstream against the main flow. Such a configuration should induce separation or increase the intensity of recirculation. In case 2, the electrodes are diverging in the downstream direction. In this case, the

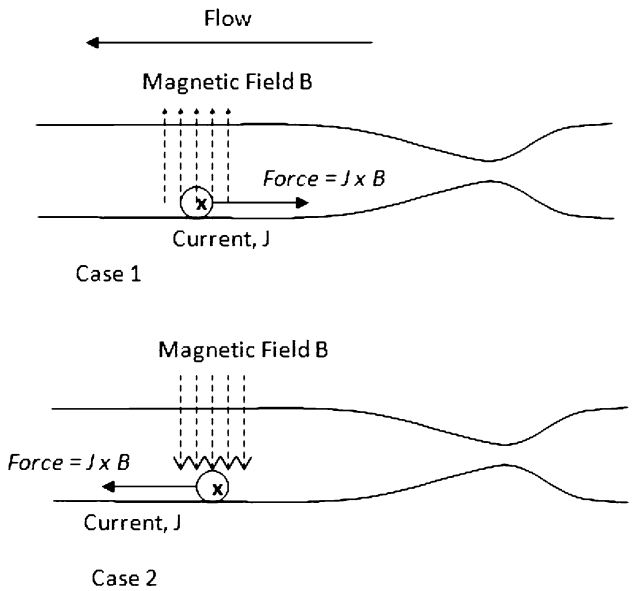

Fig. 5 Experimental configurations used in this study. Case 1: upstream plasma actuation inducing separation and case 2: downstream plasma actuation to control shockwave-induced separation

magnetic field is applied such that body force $j \times B$ forces the plasma column downstream in the direction of main flow. This configuration should cause flow attachment or a reduction in the intensity of flow recirculation.

3.2 Acetone planar laser scattering (PLS)

Acetone injection into the supersonic boundary layer perpendicular to the core flow results in the formation of fine droplets of acetone in the boundary layer, that are of reasonable size for laser sheet scattering (Bookey et al. 2005). The use of acetone PLS results in good boundary layer flow visualization in a relatively non-intrusive way (Bookey et al. 2005). This method can compliment average static pressure measurements in terms of location and size of the recirculation zone.

Figure 6 shows the setup for the acetone experiments in detail. Liquid acetone is injected a few boundary layer thickness upstream of the test section. The injected acetone stream is sheared into a cloud of tiny droplets due to the shear force along the wall in the flow. The test section is illuminated using a laser sheet from a frequency doubled ND:YAG pulsed laser. A cylindrical lens setup is used to generate the laser sheet. The laser illuminates a planar section in the wind tunnel either parallel to the test section wall, to visualize the exact location of incipient separation, or perpendicular to the test section wall, for visualization of the dimensions of the separation zone. A Princeton Instruments iCCD camera is used to image the scattered light from the acetone cloud. The optical access of the super conducting magnet from all direction inside the test section is useful for the purpose of illumination and imaging of the acetone.

4 Results

4.1 Schlieren imaging

Initial experiments were done with oblique shocks, generated by a 10 degree half-angle diamond-shaped wedge, interacting with the boundary layer on the opposing wall. The experiments show that the shockwave–boundary layer interaction is weak and does not cause the separation of incoming boundary layer. It was noted by Bookey et al. (Opaits et al. 2007) that when separation occurs the reflected shock is observed well before the shockwave hits the boundary layer due to increasing thickness of the boundary layer. In the 10 degree wedge case, Fig. 7a shows a schlieren image of the interaction zone and it is observed that the reflected shock appears after the incoming oblique shock hits the boundary layer, indicating no separation. The wall static profile shown in Fig. 8 has an essentially continuous slope with no plateau, also indicating the

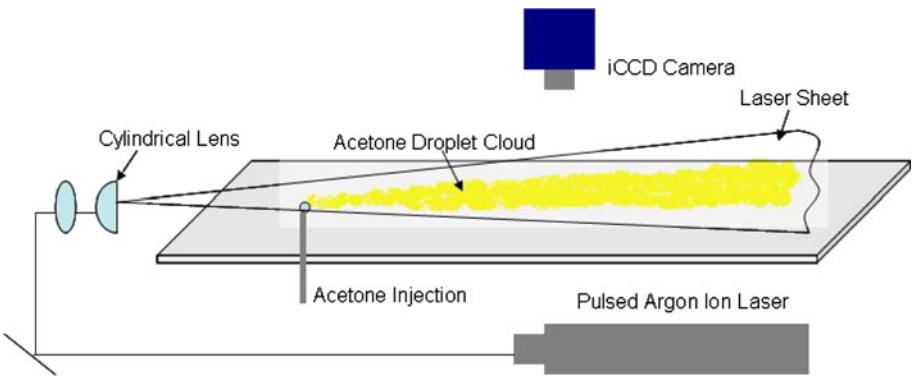

Fig. 6 Experimental setup for acetone injection and flow visualization

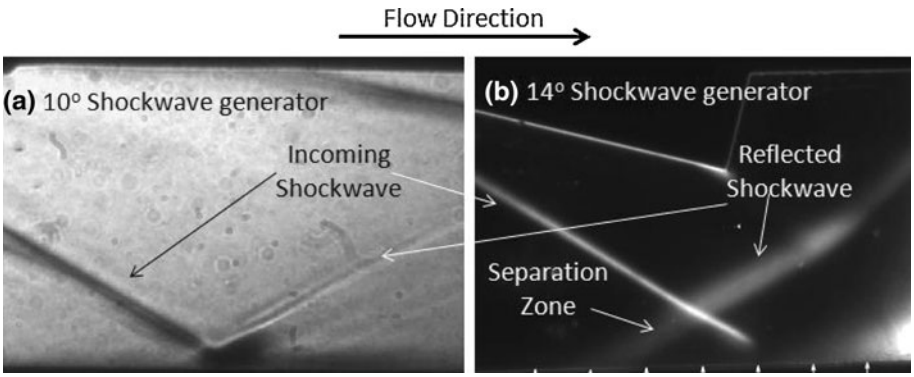

Fig. 7 Schlieren images showing shockwave–boundary layer interaction region for various shock generators

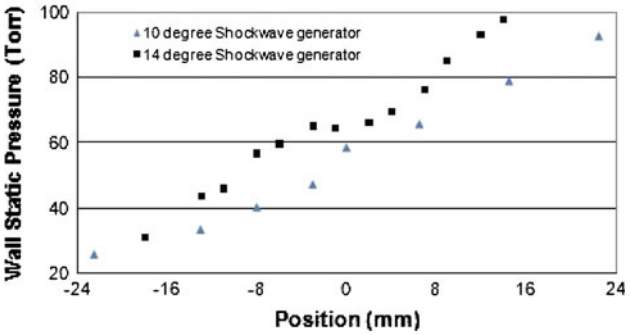

Fig. 8 Baseline static pressure profile with various shockwave generators used in the study

absence of recirculation. A final indicator that no recirculation is occurring is shown by the fact that if the local flow in the boundary layer were indeed separated and moving upstream against the direction of core flow, the plasma column should not be able to penetrate fully into the recirculation zone without magnetic field forcing. In the experiments with a high-speed camera, the plasma column is seen to convect all the way to the end of the electrodes and beyond the interaction zone without any magnetic field. This further confirms that there is no separation.

An oblique shockwave generated from a 14 degree angle diamond-shaped wedge interacting with the turbulent boundary layer, on the other hand, does induce a recirculation bubble and separation. This is verified by a schlieren image of the interaction zone in Fig. 7b, which shows that the reflected shock appears significantly upstream of the point where the incoming oblique shock hits the boundary layer. Also note that the wall static profile shown in Fig. 8 has a plateau in the middle, which indicates that the flow is separated due to the interaction. Figure 9 shows images of the moving plasma column in the absence of an applied magnetic field. Very short exposure images show the plasma column to be about 1 mm in diameter. At longer exposure times (as in this image) what we see are a blurred plasma column images as the plasma column travels along the electrodes. By the extent of the blurred image and knowledge of the exposure time, the speed of the plasma column along the electrode can be deduced. Figure 9a was taken when there was no wedge to generate the shock, thus there is no separation zone. In this figure, it is clearly seen that plasma column moves to the end of electrodes because the flow is moving downstream. The plasma column eventually extinguishes because of finite length of electrodes and reignites at the shortest distance. In Fig. 9b, the 14 degree wedge is present and the boundary layer flow is separated. In this image, it is seen that the plasma column cannot move to the end of electrodes. This is because the local flow in the separated region is reversed and is moving upstream.

In the case of the weak shockwave–boundary layer interaction, generated using 10 degree wedge, separation can be induced when the plasma column is forced upstream. This is observed in experiments with the electrode geometry shown in case 1 (Fig. 5). The static wall pressure profile shown in Fig. 10 indicates that when plasma actuation is done in the upstream direction, recirculation is induced. An increase in current or magnetic field increases the interaction parameter and results in stronger recirculation; this effect is illustrated in Fig. 10b. When a downstream force is applied using the electrode and magnetic field configuration shown in case 2; the static pressure profile shows negligible change for non-recirculating flows.

In the case of oblique shockwave generated using a 14 degree wedge, there exists strong separation and upstream plasma actuation (case 1) in this setup results in increased recirculation as expected. Downstream actuation at low current, less that 80 mA, does not show a significant change in the static wall pressure profile, but schlieren images do show some important change in the structure of the recirculation zone. Figure 11 shows two schlieren images taken with and without an applied magnetic field but with constant plasma power input. The length l, marked by the arrows in the two right hand images, is the distance over which the incoming oblique shock extends after interacting with the first of the compression waves from thickening boundary layer due to separation. It can be seen that in the presence of a magnetic field (MHD—flow interaction) this length is more than in the absence of a magnetic field (Fig. 11a, b). As the actuation current is

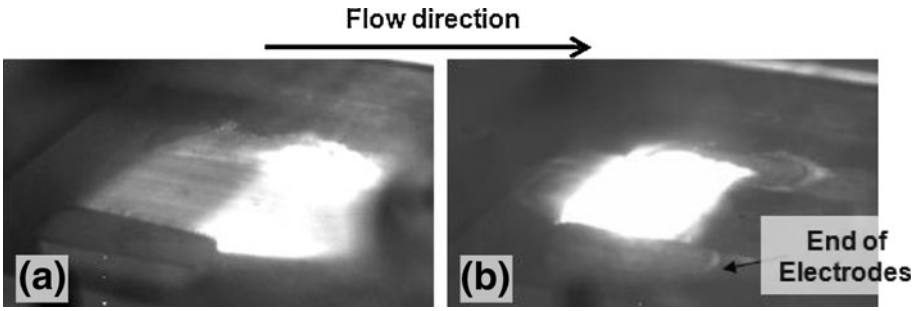

Fig. 9 Images of traveling plasma column in the absence of magnetic field. **a** With no separation and **b** with separation induced by 14 degree shockwave generator

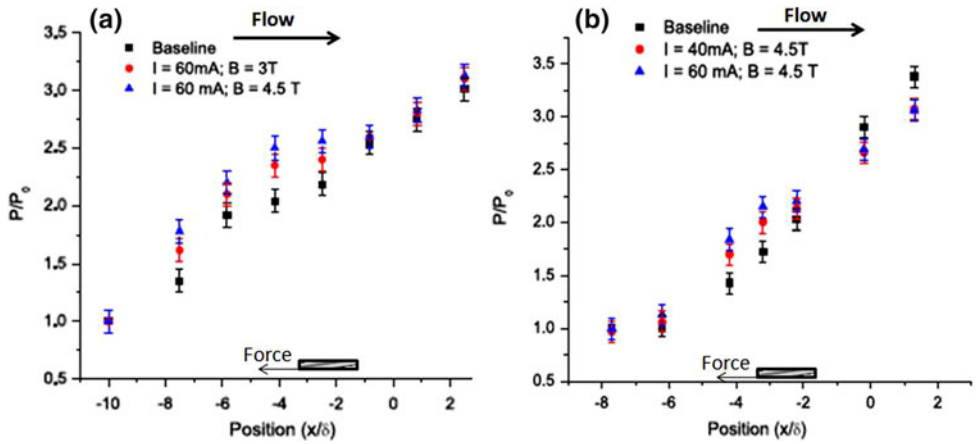

Fig. 10 Effect of upstream plasma actuation when shockwave is weak and does not induce separation (case 1); **a** at different magnetic field strengths and **b** at different current flowing through the actuator

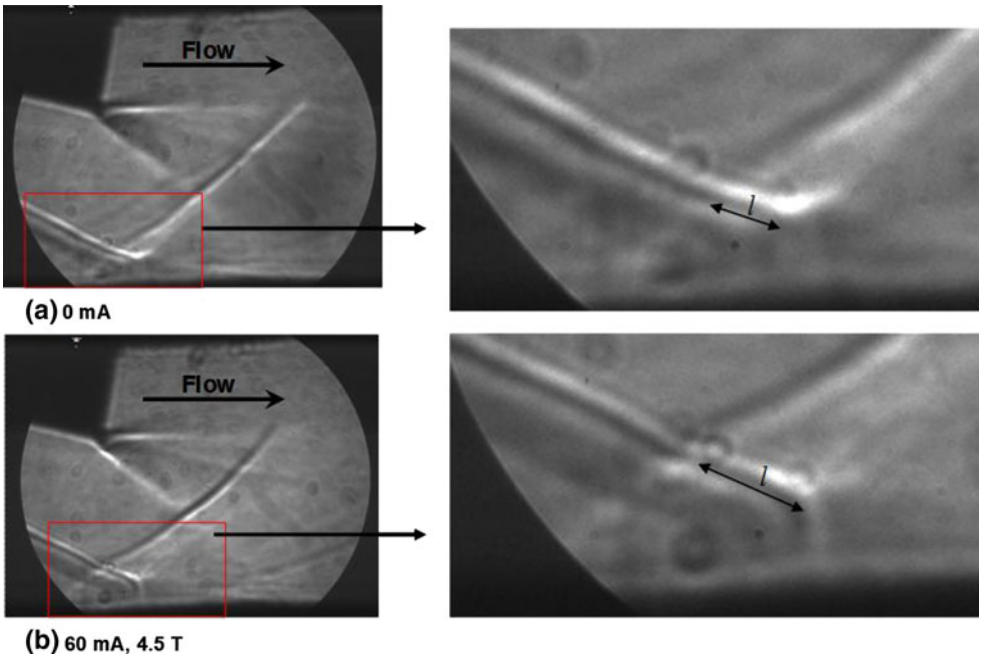

Fig. 11 Schlieren images of the separated interaction zone. **a** Without plasma actuation and **b** with downstream plasma actuation

further increased above 80 mA, the effect of non-thermal plasma actuation becomes more apparent and results in significant modification of the static wall pressure profile. In Fig. 12a, the no actuation or baseline wall static pressure profile is compared with plasma actuation at 3 Tesla and various actuation currents. The shaded area shows the location of plasma actuation. In Fig. 12b, the effect of the change of magnetic field strength is shown. In Fig. 12a, the slope increases rapidly as actuation current is increased from 130 to 200 mA compared with the baseline. Further increase in actuation current, to 250 mA, results in a reduced slope of the wall static pressure profile. This is possibly due to the fact that joule heating from the plasma zone enhances the recirculation bubble. In the graph in Fig. 12b, it is clear that at high magnetic fields in excess of 3 Tesla, there is a significant impact of plasma actuation but even at 1 Tesla magnetic field strength, some reduction in separation is observed. At 200 mA and 3 Tesla actuation, the point of incipient separation (the point to which the downstream high pressure penetrates upstream in the boundary layer interaction zone) is displaced about 10 mm or about 2 boundary layer thickness downstream. For 1 Tesla field strength at the same current, the downstream displacement is on the order of 4mm or close to one boundary layer thickness.

A good amount of information of is obtained from the average wall static pressure profile as shown above. It can accurately predict the location of high pressure penetration point upstream from shockwave impingement point, and it also provides fair estimation of strength of recirculation from the slope of the curve. But these are indirect measurements of the recirculation and separation structure. To understand the effect of plasma actuation on the interaction zone and the exact flow structure, direct flow visualization

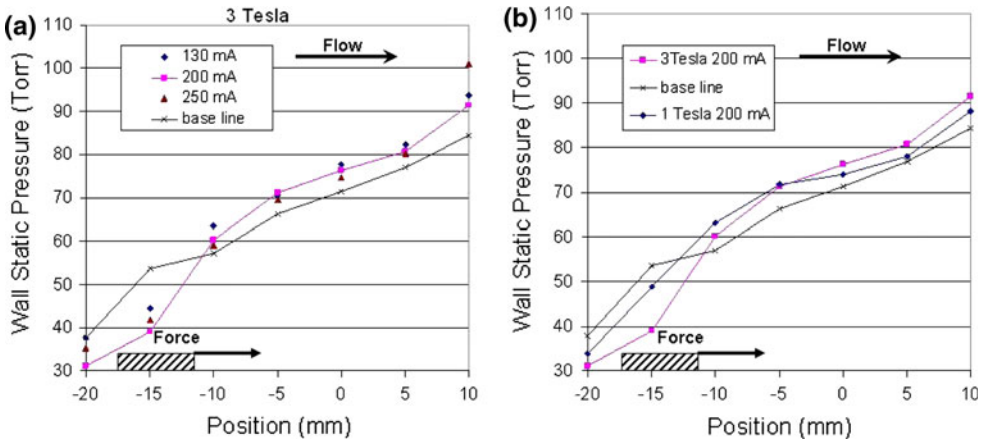

Fig. 12 Effect of downstream plasma actuation with shockwave-induced separation (case 2); **a** at different actuation currents and **b** at different applied magnetic field strength

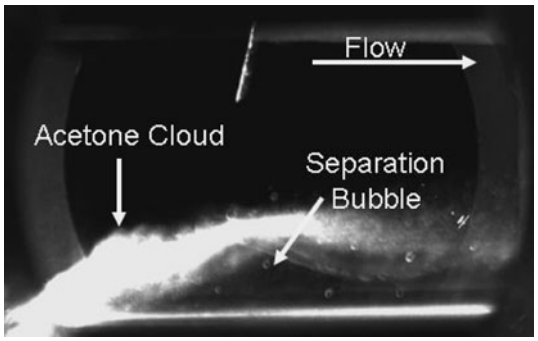

Fig. 13 Side view of the separation as visualized by acetone PLS

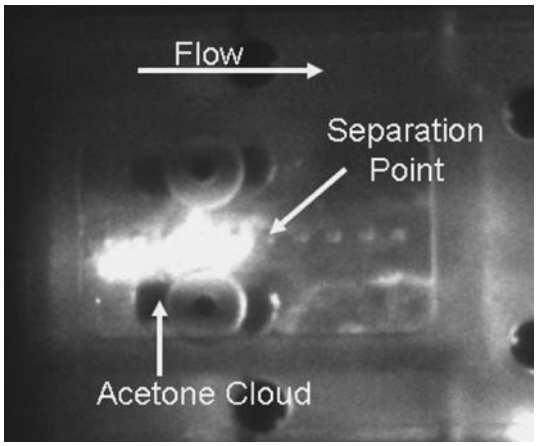

Fig. 14 Top view of the separation as visualized by acetone PLS

is done using acetone PLS imaging. These experiments are performed to visualize the flow structure and are reported in the next section. Also a detailed numerical model of the shockwave–boundary layer interaction has been developed to study the effect and reported elsewhere (Kalra et al. 2009).

4.2 Acetone PLS visualization

Acetone visualization of the shockwave–boundary layer interaction is done using liquid acetone injection into the boundary layer, perpendicular to the core flow upstream of the interaction region. Figure 13 shows the side view of the acetone cloud when the laser sheet illuminates a plane perpendicular to test section wall on which the oblique shockwave impinges. This flow shows the path of the boundary layer flow around the separation bubble. With this technique, the extent of separation and also the height of the recirculating bubble can be determined with good accuracy. The injection point is located upstream at 12δ to get stable acetone flow rate. The standard deviation of the acetone scattering intensity fluctuations is about 10 percent of the average intensity.

Figure 14 shows the top view of the acetone cloud in the interaction zone. In this case, the laser sheet is injected parallel of the test section wall on which the shockwave impinges. The distance between the test section wall and laser sheet is about 1mm. As the boundary layer flow separates, the acetone cloud goes around the separation bubble and almost no acetone penetrates into the recirculation zone when separation occurs. This view shows the location of the separation point. The data obtained from acetone PLS images shows that the separation zone is about 10 mm wide and is well upstream of the shock impingements point.

The impinging shockwave and the separation bubble are non-stationary and the low frequency of motion is of the order of $(0.007 - 0.013)U_\infty/\delta$ (Wu et al. 2005). Due to this oscillation, the images collected from various experiments are averaged before comparing for determining the effects of plasma actuation. To average the data, more than 100 images were collected for each experiment and then statistically relevant images were selected from the group and averaged over turbulent fluctuations to get an average image of the separation bubble. Experiments are done initially at baseline conditions without any plasma actuation current, giving the structure of the flow as shown in

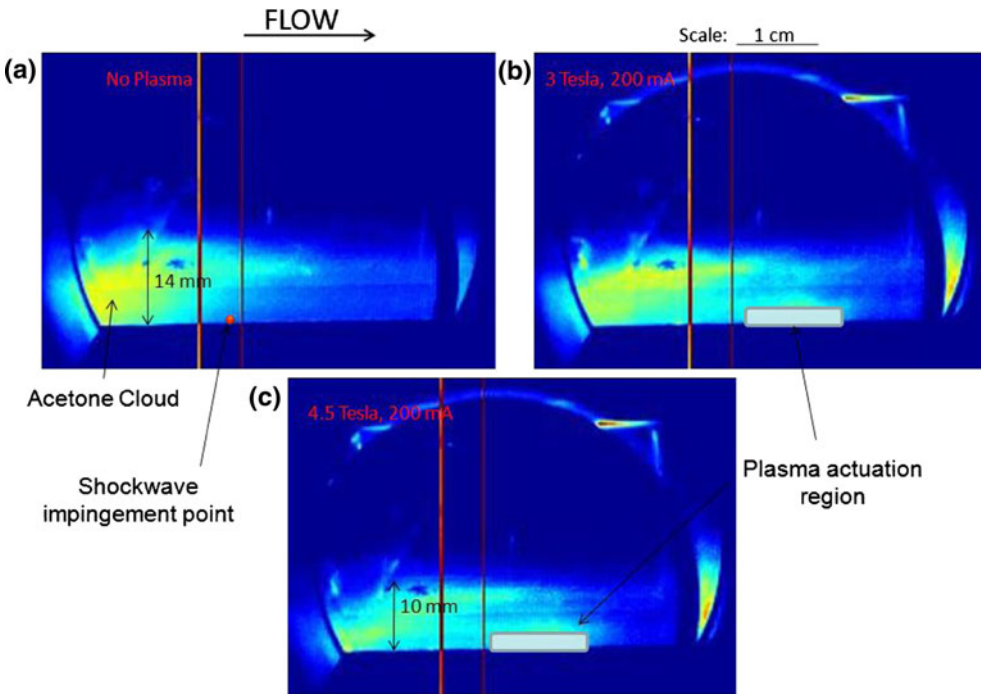

Fig. 15 Time averaged side view of the separation as visualized by acetone PLS. **a** Base line case with no plasma actuation, **b** plasma actuation at 3 Tesla and **c** plasma actuation at 4.5 Tesla

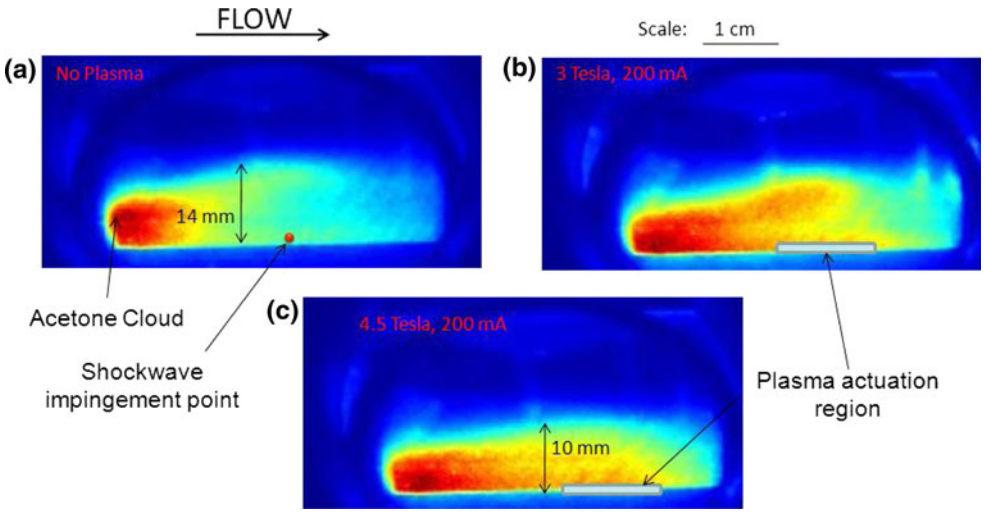

Fig. 16 Time averaged side view of the separation as visualized by acetone PLS with the shock impingement location moved downstream by 2δ, **a** base line case with no plasma actuation, **b** plasma actuation at 3 Tesla and **c** plasma actuation at 4.5 Tesla

Fig. 15a. Figure 15b shows the flow structure at a high actuation current of 200 mA and a moderate magnetic field of 3 Tesla. As the field strength is increased from 3 to 4.5 Tesla the flow structure is modified more rapidly as shown in Fig. 15c.

As the shockwave impingement point is moved farther downstream by 2δ, the effectiveness of the plasma actuation increases. This is shown in Fig. 16. Figure 16a, shows the baseline case without plasma actuation and Fig. 16b and c show averaged images of flow structure with plasma actuation, as the magnetic field strength is increased to 4.5 Tesla, the acetone cloud can now penetrate inside the separation bubble. The imaging is done through a 532 nm optical filter at 1 μs exposure time, which ensures that the intensity represents the acetone cloud only and no luminosity due to plasma emission or acetone fluorescence are captured in the image.

Figure 17 shows the top view of the acetone cloud when the illuminating plasma sheet is 2 mm away from the test section wall. In Fig. 17a when no plasma actuation is applied the separation and reattachment points are clearly identified. As the plasma actuation is increased, the acetone cloud penetrates into the separation zone and is visible throughout the separation region, as seen in Fig. 17b. This gives further evidence that magnetically driven plasma actuation increases the momentum of the incoming boundary layer and reduces the strength of the

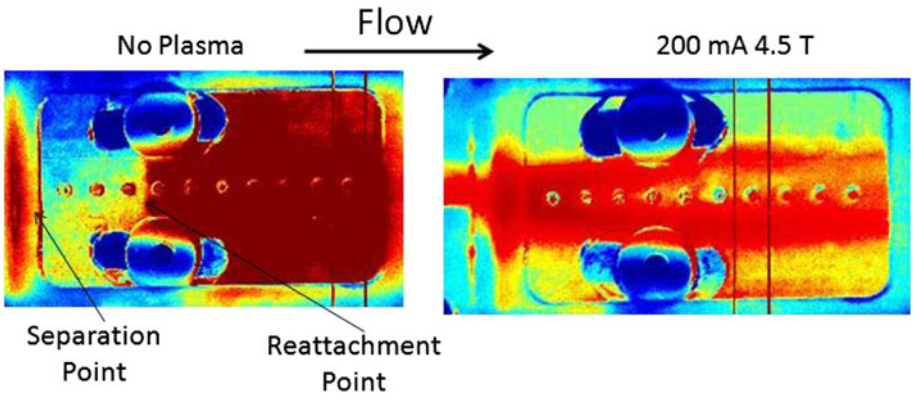

Fig. 17 Time averaged top view of the separation as visualized by acetone PLS. **a** Base line case with no plasma actuation, **b** plasma actuation at 4.5 Tesla

separation bubble induced by the shockwave–boundary layer interaction.

5 Conclusions

This experimental study of shockwave–boundary layer interaction control performed at Mach 2.6 demonstrates that a magnetically driven surface discharge can provide effective control of the boundary layer structure. A weak shockwave generated from a 10 degree wedge, when reflected from a turbulent boundary layer, does not result in separation, but with upstream action of the plasma actuator, separation can be induced in the boundary layer flow with a significant change in wall static pressure profiles. For a stronger shockwave generated from a 14 degree wedge, a recirculation zone is induced in the boundary layer and the flow is separated. In this case, the structure of the shock-wave–turbulent boundary interaction (STBLI) is modified with a weak downstream force from the plasma actuator, leading to a reduction in the slope of the thickening boundary layer at low actuation currents up to 80 mA. Further increase in actuation current results in the reduction of the size and strength of recirculation when magnetic field strengths greater than 1 Tesla are applied. With magnetic field strengths of 3 Tesla and at currents greater than 80 mA, separation could be fully suppressed. Acetone laser scattering experiments show the flow structure of the interaction region and the reduction in the size of recirculation with plasma actuation. Static wall pressure measurements show the extent of recirculation in shockwave–boundary layer interaction region and the effect of plasma control. Joule heating effects become dominant at actuation currents above 250 mA mitigating the effect of non-thermal flow control.

Acknowledgments This work was supported by the AFOSR Unsteady Aerodynamics and Hypersonic Program, by a DARPA STTR program with CMI Inc., and by an AFOSR SBIR program (also with CMI. Inc.).

References

Bookey P, Wyckham C, Smits A (2005) Experimental investigations of Mach 3 shock-wave turbulent boundary layer interactions, AIAA 2005-4899. In: 35th AIAA fluid dynamics conference and exhibit, Toronto, 6–9 June

Chapman DR, Kuehn DM, Larson HK (1958) Investigation of separated flows in supersonic and subsonic streams with emphasis on the effect of transition. NACA Rept. 1356

Delery J, Marvin JG (1986) Shockwave boundary layer interactions, AGARD-AG-280

Dolling DS (2001) Fifty years of shock-wave/boundary-layer interaction research: what next? AIAA J 30(8):1517–1531

Fujino T, Funaki I, Mizuno M, Sugita H, Ishikawa M (2004) Numerical studies of influences of hall effect on MHD flow control around blunt body OREX. In: 35th AIAA plasmadynamics and lasers conference, Portland, 28 June–1 July, AIAA 2004-2561

Gaitonde DV (2008) High-speed magnetohydrodynamic flow control analyses with three-dimensional simulations. J Propuls Power 24:946

Jesse L, Nishihara M, Adamovich I, Samimy M (2009) High-lift airfoil trailing edge separation control using a single dielectric barrier discharge plasma actuator. Exp Fluids 0723-4864

Kalra CS, Shneider MN, Miles RB (2009) Numerical study of boundary layer separation control using magnetogasdynamic plasma actuators. Phys Fluids 21:106101. doi:10.1063/1.3233658

Kral L (1999, Spring) Active flow control technology. ASME Fluids Engineering Division Newsletter, pp 3–6

Lin JC (2002) Review of research on low-profile vortex generators to control boundary layer separation. Prog Aerosp Sci 38:389–420

Lineberry JT, Bityurin VA, Bocharov AN (2002) Analytical study of MHD flow interaction around a right circular cylinder in transverse hypersonic flow. In: 33rd Plasmadynamics and lasers conference, Maui, 20–23 May, AIAA-2002-2112

McCormick DC (1992) Shock-boundary layer interaction control with low-profile vortex generator s and passive cavity. In: AIAA Paper 92-0064, 30th AIAA Aerospace Sciences Meeting and Exhibit, Reno, January 6–9

Nishihara M, Jiang N, Rich JW, Lempert WR, Adamovich IV (2005) Low-temperature supersonic boundary layer control using repetitively pulsed magnetohydrodynamic forcing. Phys Fluids 17:106102

Opaits DF, Neretti G, Likhanskii AV, Zaidi S, Shneider MN, Miles RB, Macheret SO (2007) Experimental investigation of DBD plasma actuators driven by repetitive high voltage nanosecond pulses with DC or low frequency sinusoidal bias. In: 38th Plasma

dynamics and lasers conference, Miami, 25–28 June, AIAA Paper No. 2007-4532

Raizer YP (1997) Gas discharge physics. Springer, Berlin

Shang JS, Kimmel R, Hayes J, Tyler C, Menart J (2005) Hypersonic experimental facility for magnetoaerodynamic interactions. J Spacecr Rockets 42(5), September–October

Wu M, Bookey P, Martin MP, Smits AJ (2005) Analysis of shockwave/turbulent boundary layer interaction using DNS and experimental data. In: 43rd AIAA aerospace sciences meeting and exhibit, Reno, 10–13 January, AIAA Paper No. 2005-0310